


Influence of Homogenization and Annealing Temperatures on the Microstructure, Mechanical Properties, and Passive Properties of Cold Rolled 2205 Duplex Stainless Steel

Raphael F. Assumpção^{a*} , Ricardo A. Júnior^b, Amanda P. Silva^b, Francislayne L. Dias^a,
Dagoberto B. Santos^a, Dalila C. Sicupira^b

^aUniversidade Federal de Minas Gerais, Departamento de Engenharia Metalúrgica e de Materiais, 31270-901, Belo Horizonte, MG, Brasil.

^bUniversidade Federal de Ouro Preto, Departamento de Química, Campus Morro do Cruzeiro, 35400-000, Ouro Preto, MG, Brasil.

Received: February 8, 2022; Revised: July 12, 2022; Accepted: July 13, 2022

The effects of homogenization, cold working, and subsequent annealing treatment were studied on the microstructural evolution, mechanical properties, and passive properties of duplex stainless steel (DSS). A hot-rolled 2205 DSS was subjected to two processing routes. In one, the DSS goes through an extra homogenization step at 1100 °C for 1800 s before cold rolling. After cold deformation (~75%) the specimens were isothermally annealed at 900, 1000, and 1100 °C for 180 s. The microstructure evolution was studied by optical microscopy (OM), scanning electron microscopy (SEM) and X-ray diffraction (XRD). Mechanical properties were evaluated by microhardness and tensile tests. The electrochemical behaviors were investigated by potentiodynamic measurements, electrochemical impedance spectroscopy (EIS) and Mott-Schottky analysis (MS). Chemical composition of the lowest corrosion resistant passive film was assessed by X-ray photoelectron spectroscopy (XPS). Homogenization before cold rolling lowered strain hardening, slowing the microstructural transformation process. The thermomechanical process did not change the semiconductor type of the passive films. However, grain refinement after annealing improved the corrosion resistance in borate buffer solution. Cold rolling significantly decreased the corrosion resistance. The passive film of the specimen homogenized before cold rolling had the lowest corrosion resistance and high amounts of Cr(OH)₃ and FeO.

Keywords: Corrosion, Annealing, Duplex stainless steel, Mechanical properties, Passive properties.

1. Introduction

Duplex stainless steels (DSS) are complex alloys with a two-phase microstructure composed of austenite (γ) and ferrite (α). DSS are highly important engineering materials widely used in various industrial sectors, such as oil and gas (pipelines and storage tanks), desalination (evaporators and pumps), pulp and paper (digester and bleaching reactors) industries, due to their generally high corrosion resistance combined with high strength^{1,2}.

The high corrosion resistance of DSS is primarily attributed to the passive film formed on the surface³. This so-called passive film is generally described as a few nanometers-thick oxyhydroxide layers, composed mainly of Cr(III) species in the inner layer and Fe(III) species in the outer layer^{4,5}. The composition, thickness, structure, and electronic properties of the passive films affect the corrosion resistance of DSS⁶.

The electrochemical behavior of DSS depends on the constituent phases and their chemical compositions⁷. In DSS, alloying elements are partitioned between the austenite and ferrite phases: Ni and N contents are preferentially partitioned in the austenitic phase while, Cr and Mo contents

are enhanced in the ferritic phase⁸⁻¹¹. The link between the chemical composition of the austenite and ferrite phases and the chemical composition of the oxide layer formed on both phases is a key point relative to the passivity of DSS⁵.

In addition to the chemical composition, an annealing treatment is another important factor influencing the corrosion resistance of DSS^{10,12}. With the given chemical composition, varying heat treatment temperatures can change the proportion of the ferrite and austenite phases and adjust the redistribution of alloying elements in the two phases, leading to a variation in the corrosion resistance of each one^{11,12}.

Though the homogenization in DSS serves the purpose of dissolving unwanted phases, it is often associated with grain coarsening, possible austenite-to-ferrite phase transformation, and changes in phase-specific chemistry. Naturally, such changes in the microstructures are expected to reflect on the corrosion performance¹³.

On the other hand, the instability of the ferrite phase, due to improper heat treatment temperature, may cause the precipitation of deleterious secondary phases, such as the sigma phase in duplex stainless steels, which causes the Cr and Mo elements to be depleted in the regions adjacent to the matrix due to their consumption in solid solution, reducing the corrosion resistance and mechanical properties¹⁴⁻¹⁶.

*e-mail: raphaafraanca@hotmail.com

Among the various compositions of duplex stainless steels, the most used commercially is UNS S32205/S31803 (22Cr-5Ni-3Mo-0.16N), also known as SAF 2205, or just 2205. This steel normally goes through at least one hardening route (plastic deformation), recovery, and recrystallization.

During the last few years, the effects of rolling, solution annealing, and annealing temperatures on the microstructural features and corrosion resistance of DSS have been intensively investigated^{12,13,17-23}. Mondal et al.¹³ reported a decrease in corrosion resistance after grain coarsening during solution annealing of a super duplex stainless steel at 1050 °C for different times. According to Zhang et al.¹² annealing a hot rolled 2205 DSS from 975 to 1075 °C for 2h leads to a more homogeneous microstructure, and the pitting corrosion resistance increases. Malta et al.²⁴ studied the influence of annealing temperature on pitting resistance of a 2304 DSS. The obtained results showed that pitting resistance is considerably increased by annealing the alloy from 900 °C to 1100 °C. Jinlong et al.¹⁸ investigated the corrosion properties of passive films formed on coarse grained and ultrafine grained 2205 DSS and concluded that severe cold rolling can improve the corrosion resistance of the 2205 DSS in borate buffer solution.

Although the effects of rolling, solution annealing, and annealing temperatures have been extensively reported, there is a limited amount of work on the effect of short time annealing after severe cold rolling aimed at grain refining in the passive film characteristics of duplex stainless steels. This work aims to study the corrosion resistance of the passive film formed in DSS 2205 in borate solution after homogenization, cold rolling and annealing at 900 °C, 1000 °C, and 1100 °C for 180 s. Also, it is intended to evaluate the effects of homogenization before cold rolling on microstructure, mechanical and corrosion resistance.

2. Materials and Methods

This study was carried out using 4 mm and 5 mm thick sheets of a hot-rolled and annealed 2205 stainless steel with the following chemical composition by mass spectroscopy in weight percent: 0.023C, 1.797 Mn, 0.037 P, 0.001 S, 0.278 Si, 22.52 Cr, 5.54 Ni, 3.25 Mo, 0.148 Cu, 0.157 N, and Fe balance.

The as-received (AR) samples went through two processing routes, a non-homogenized route, and a homogenized route. The cold rolling procedure was performed in a Fröhlung laboratory rolling mill in 6.5 m/min velocity. In the non-homogenized route, the 4.0 mm thick as-received (AR) sheet was cold rolled (CR) to a thickness reduction of 75%, thus achieving a thickness of 1.02 mm in fourteen passes. Then, the CR samples were annealed at 900 °C, 1000 °C, and 1100 °C for 180 s and water-quenched, leading to the final products (FP1, FP2, and FP3). The homogenized route starts with an additional homogenization (H) step, at 1100 °C for 1800 s, before cold rolling, leading to as-received homogenized (ARH). The homogenized cold rolled (CRH) sample was processed in twelve passes ($\epsilon = 0.80$) to a thickness of 1.11 mm, after annealing it led to the homogenized final product (FPH1, FPH2, and FPH3) samples. The phase volume fraction as a function of temperature was calculated using

the Thermo-Calc software for the 2205 DSS studied in this work, as shown in Figure 1.

The samples for the microstructural analysis were characterized along the longitudinal section using optical (MO) and scanning electron microscopy (SEM). For the OM and SEM analysis, the samples were ground with SiC abrasive papers with grit up to 1000#, polished with fine diamond paste (9, 6, and 1 μm), and then electrolytic etched in 10% oxalic acid solution at 4.5 V for 5.0 s with oxalic acid and Beraha etchant, respectively.

Regarding the identification of the phases, X-ray diffraction (XRD) was performed in a PANanalytical Empyrean diffractometer using a Cu K α radiation, operating at 45 kV and 45 mA, and with a step size of 0.02° and time per step of 1 s. The diffraction patterns have an angular range of 35° through 100°. To consider the influence of texture, the phases were quantified based on the integration of the areas of each diffraction peak of the principal planes, following the methodology used by Knutsson et al.²⁵, according to the Dickson²⁶ approach.

The evolution of the mechanical properties related to the microstructural changes was evaluated by hardness and tensile tests. Vickers hardness (HV) was measured using a Future Tech FM-700 microhardness instrument using a dwell time of 10 seconds and a load of 300 gf. The mean HV values of each sample were calculated from twenty random measurements. The tensile tests were carried out according to ASTM A370-14. The uniaxial tensile tests were carried out in triplicate using an Instron 5985 at a deformation speed of 1.0 mm min⁻¹. The uniaxial tensile tests were carried out in triplicate in an Instron 5985 at a deformation speed of 1.0 mm min⁻¹ using the Blue Hill software for data acquisition. The specimens were taken from the RD-TD plane in the RD direction using the dimensions of the ASTM A370-14 subsize, as shown in Figure 2.

The electrochemical measurements were performed with a potentiostat Autolab PGSTAT302N using a three-electrode cell. A platinum plate and an Ag/AgCl (sat.) were used as the counter and the reference electrodes, respectively. The specimens acting as working electrodes were embedded in acrylic resin. The contact region between the sample and

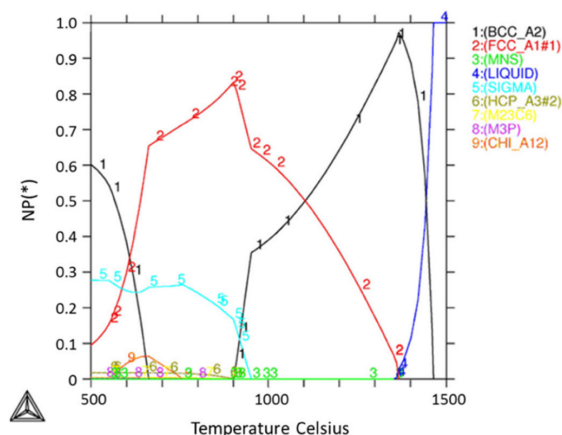


Figure 1. Phase fraction as a function of temperature calculated by using the Thermo-Calc software for the 2205 DSS.

the acrylic resin was sealed with araldite epoxy adhesive, to avoid crevice.

For the electrochemical analysis, DSS plates were cut into 10 mm x 10 mm and ground with SiC paper up to 600#, cleaned in ethanol and distilled water, and then dried in air. The electrochemical measurements were initiated after 60 min at the open circuit potential (OCP) stabilization at 25 °C. To ensure good reproducibility, a minimum of three sets of measurements for each sample was taken and an average value was considered in pH 9 borate buffer solution (0.05 M H_3BO_3 e 0.075 M $Na_2B_4O_7 \cdot 10H_2O$), which was extensively used to investigate the passivity of stainless steels in previous works²⁷⁻³².

Potentiodynamic polarization experiments were performed to determine the anodic potential range for the passive film formation. A scan rate of 0.167 mV s^{-1} was used in the anodic direction starting from the open-circuit potential, OCP, to the potential at which the current density reached 1.0 mA cm^{-2} .

To study the semiconductor characteristics of the passive film on 2205 DSS Mott-Schottky analysis was carried out. The MS plots were obtained by sweeping in a negative direction at a frequency of 1000 Hz with an amplitude signal of 10 mV, the potential range from $+200 \text{ mV}_{Ag/AgCl}$ to $-800 \text{ mV}_{Ag/AgCl}$ with a potential step of 50 mV. This procedure was adopted to “freeze-in” the potential-dependent defect structure and barrier layer thickness³.

The electrochemical impedance spectroscopy (EIS) measurement to the analysis of the electrochemical behavior of the oxide film formed on the specimen surface. EIS tests were carried out at open-circuit potential conditions and AC potential with the amplitude of 10 mV rms and a frequency range of 100 kHz to 5 mHz. The acquired impedance spectra are presented as Nyquist plots and interpreted in terms of equivalent electrical circuits using the ZView (Scribner Assoc.) program.

The chemical composition of the surface films formed at the middle of the passive region for the specimen cold rolled after the homogenization step was investigated with X-ray photoelectron spectroscopy (XPS). For the formation of passive film, the specimen was pretreated cathodically at $-0.8 \text{ V}_{Ag/AgCl}$ applied for 0.5 h to remove the native oxide film and then polarized in the borate solution at $+0.6 \text{ V}_{Ag/AgCl}$ for 2 h. Then, the samples were subsequently transferred into the AMICUS XPS instrument with a monochromatic Al K α radiation source with a pass energy of 25 eV at a step size of 0.1 eV. The C 1 s peak from adventitious carbon at 284.8 eV was used as a reference to correct the charging shifts. XPS Peak 4.1 software was used to fit the XPS experimental spectra, which contains the Shirley background subtraction and Gaussian–Lorentzian tail function, to achieve better spectra fitting.

3. Results and Discussion

3.1. Microstructure evolution

The phase change investigated by X-ray diffraction (XRD) of the 2205 DSS samples before the annealing process is illustrated in Figure 3. The ferrite (α) and austenite (γ) phases are detected in as-received 2205 DSS (AR) by XRD owing to their different crystal structure. Besides, intense

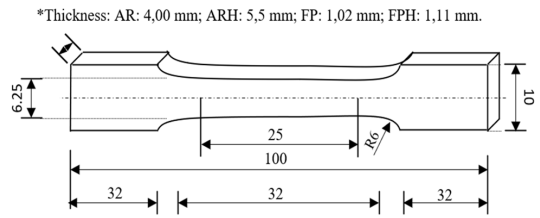


Figure 2. Schematic illustration of the specimens for tensile test.

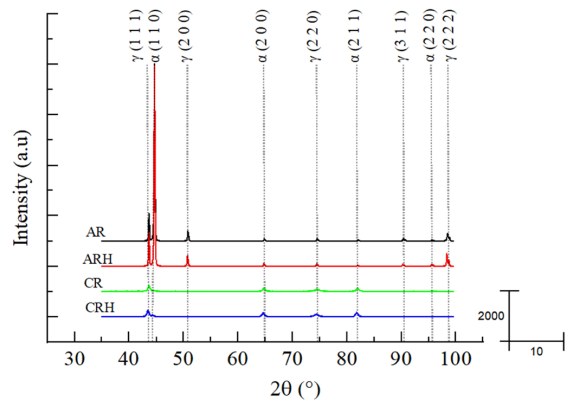


Figure 3. X-ray diffraction patterns of 2205 DSS (a) AR, ARH, CR, and CRH samples.

(110) α and (111) γ principal peaks were observed in the AR and ARH samples. The XRD patterns of cold rolled samples (CR and CRH) do not detect any other phases.

Moreover, after cold rolling, the intensities of the diffraction peaks of ferrite and austenite phases significantly change. It can be mentioned that the strain-induced martensite (SIM) could be formed, and it has the same crystallographic parameters as the ferrite, so ferrite and α' -martensite peaks are coincident. Recent studies have shown a consistent decrease in austenite with increased deformation as indicative of SIM^{18,33-38}. Furthermore, studies indicate that the peak (200) γ disappearance after cold rolling is due to the SIM formation^{20,35,39,40}. Peaks of ϵ -martensite were not found in any deformed specimen.

After annealing, α' -martensite is transformed to austenite again. XRD pattern of the annealed samples (Figure 4) showed sharp peaks for austenite and ferrite with evidence of the sigma phase annealing at 900 °C. The sigma phase under this condition was expected by Thermo-Calc software (Figure 1). It can be noticed that (200) α e (220) γ peaks observed in the FP and FPH samples are close to the (110) α and (111) γ principal peaks, suggesting texture formation in both phases²⁰. The volume fractions of the phases are listed in Table 1.

The increase of γ volume fraction after cold rolling, is related to the reverse transformation of the α into γ by a shear mechanism, as reported by Forgas et al.⁴¹ and Paula Inácio et al.⁴². After annealing at 900 °C, the γ phase reached

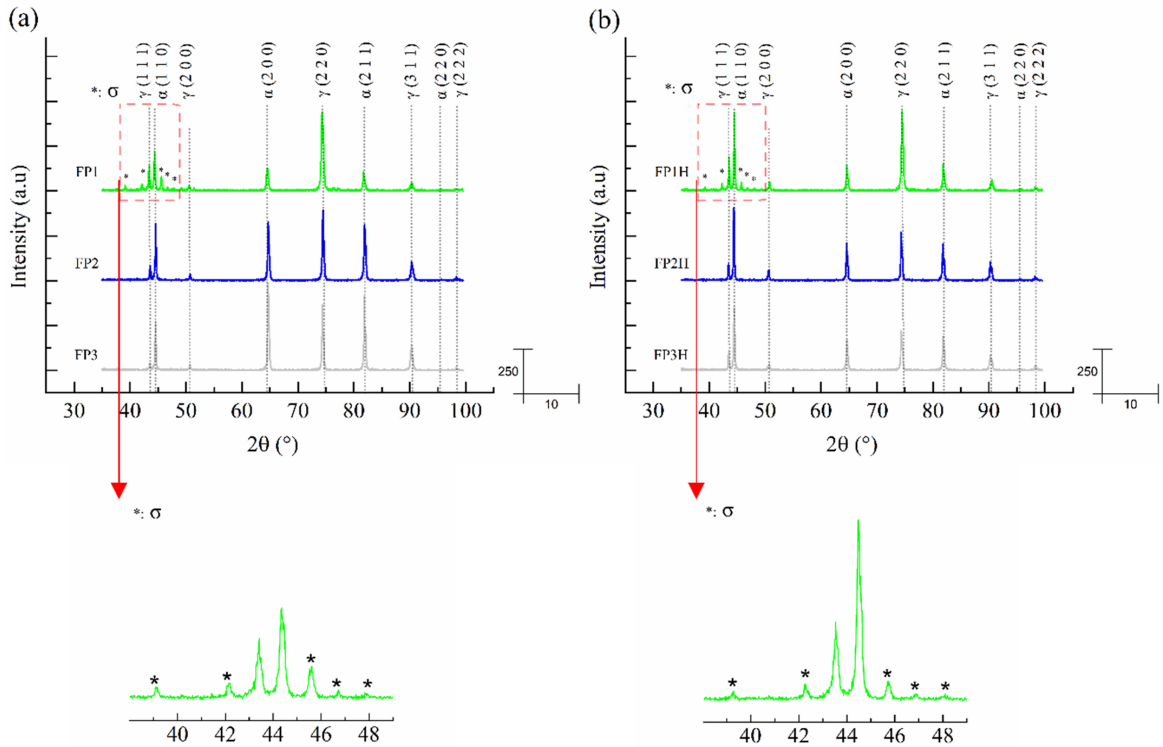


Figure 4. X-ray diffraction patterns of the annealed 2205 DSS (a) FP1, FP2, and FP3 samples and (b) FPH1, FPH2, and FPH3.

Table 1. Phase volume fraction, V_v (%), of 2205 DSS specimens.

	AR	CR	FP1	FP2	FP3	ARH	CRH	FP1H	FP2H	FP3H
α	60	54	32	61	67	61	56	41	61	62
γ	40	46	61	39	33	39	44	54	39	38
σ	-	-	7	-	-	-	-	4	-	-

a larger volume fraction than the α phase ferrite eutectoid decomposition to σ phase and possible martensite reversion. Cold rolling of the non-homogenized specimen enhanced sigma phase precipitation. Increasing the annealing temperature intensified the ferrite peaks and, hence, the volume fraction of this phase. The tendency of measured results is consistent with the calculated results shown in Figure 1, highlighting the relationship between phase fraction and temperature.

The microstructure developed throughout the thermomechanical process of the 2205 DSS is shown in Figure 5, where ND is the normal direction and RD is in the rolling direction. The electrolytic etch with a 10% oxalic acid solution only reveals grain boundaries of the deformed microstructure.

The as-received DSS (AR) shown in Figure 5a presented a characteristic pancake-like microstructure, consisting of slightly flattened and elongated austenite and ferrite bands aligned parallel to RD, in agreement with the literature^{13,33,43-45}. After homogenization (ARH), Figure 5b, is observed the elongated banded morphology along the prior hot rolling direction, grain coarsening of both ferrite and austenite phases, and annealing twins inside the austenite bands (red arrow). According to Mondal et al.¹³, it is also expected

changes in phase-specific chemistry and uniform and local corrosion resistance.

For CR and CRH, Figure 5c,d, the microstructure became more elongated within the CR as compared to the hot-rolled samples, promoting a reduction of the α and γ lamellae thickness. Also, shear bands were observed with an inclination of about 32° (Figure 5c) and 22° (Figure 5d) concerning RD (indicated in red), being the 35° angle more frequently cited in the literature^{33,46}. Studies show that some intersections of shear bands act as the nucleation sites for α' -martensite, indicating the possible presence of α' -martensite on cold rolled (CR) and homogenized cold rolled (CRH) samples⁴⁶⁻⁵⁰. Jinlong et al.⁵⁰ study reported that α' -martensite could decrease the corrosion resistance of 2205 duplex stainless steel.

The alternating morphology of α and γ elongated along the RD is still evident after annealing (Figure 5e-j). According to Malta et al.¹⁹, the retention of the lamellar structure proves that extensive recovery occurred in the ferrite phase and that its recrystallization is not complete. Increasing the annealing temperature from 900°C to 1100°C intensified the recrystallization nucleation in both phases, but the kinetics of grain growth is relatively slow due to the constraint collisions of interphase boundaries. Annealing at 900°C

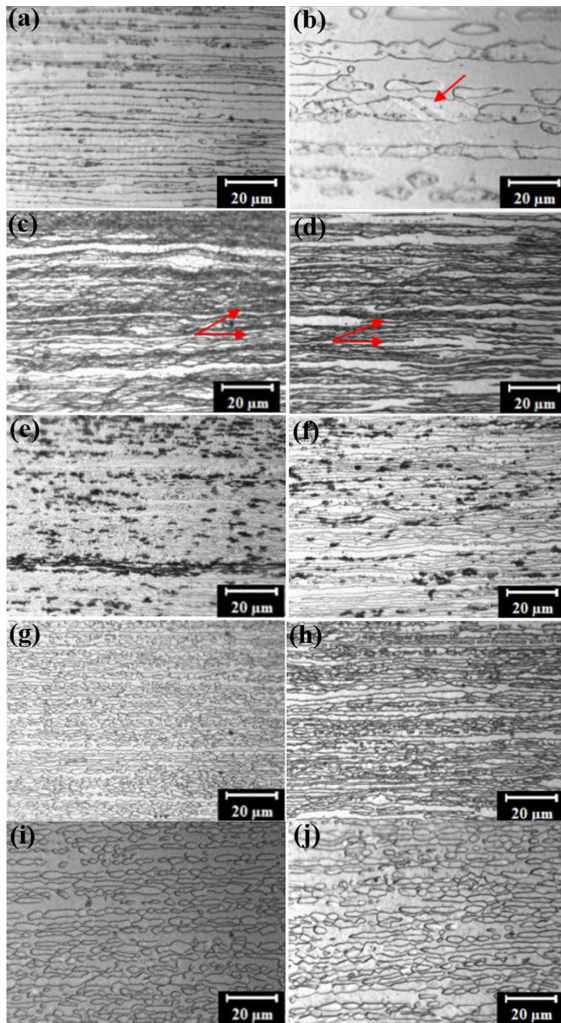


Figure 5. Optical micrographs of the samples (a) AR, (b) ARH, (c) CR, (d) CRH, (e) FP1, (f) FPH1, (g) FP2, (h) FPH2, (i) FP3, and (j) FPH3. Electrolytic etch with a 10% oxalic acid solution.

led to the precipitation of the sigma phase, as evidenced by the existence of the black spots shown in Figure 5e, f associated with localized corrosion after electrolytic etch.

The microstructure characteristics evidenced in OM micrographs are enhanced by SEM micrographs shown in Figure 6. In these micrographs, the light and the dark gray colors indicate the γ and α phase, respectively. The homogenization step led to grain coarsening. Furthermore, cold rolling resulted in significant refining of the duplex structure due to grain elongation and breaking at room temperature. The homogenization step had a clear influence on decreasing the deformation level, once the CR sample presents a lamellae thickness finer than the CRH sample.

Figure 6c,d shows some features revealed by Beraha etchant highlighting the possibility of SIM formation, as indicated by red arrows. Those same features were observed by Breda et al.⁴⁷ after cold rolling a 2205 DSS with 35% and 65% thickness reduction. The structural modifications inside the austenitic region were associated with SIM formation or possible etching differences inside the same phase by

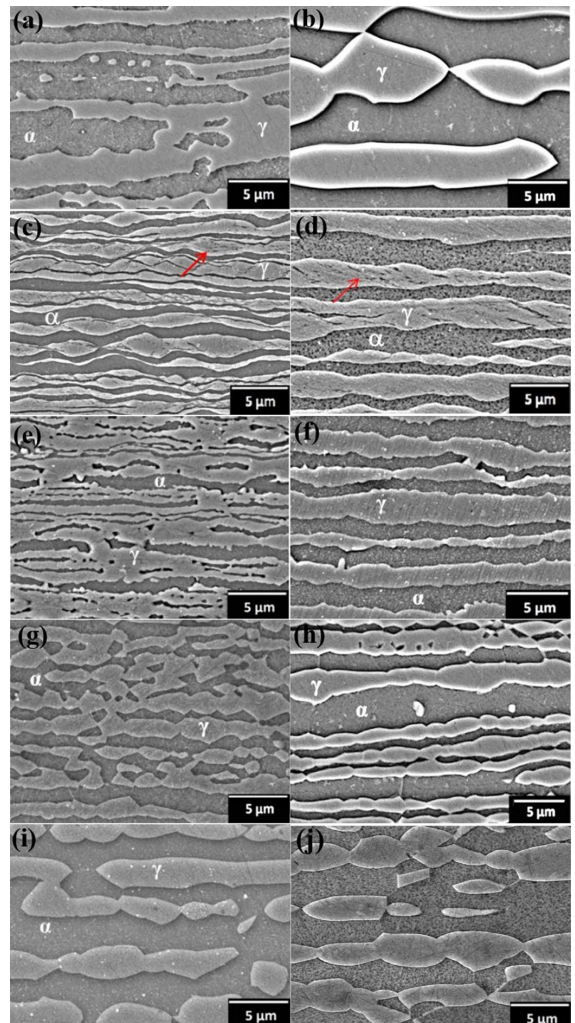


Figure 6. Micrographs of the samples (a) AR, (b) ARH, (c) CR, (d) CRH, (e) FP1, (f) FPH1, (g) FP2, (h) FPH2, (i) FP3, and (j) FPH3. Etched with Beraha etchant.

greater anodic potential than the surrounding austenite due to cold deformation.

Mendonça et al.⁵¹ observed similar modifications after annealing a lean duplex stainless steel (LDSS) at 650 °C and associated with the possibility of the transformation/reversion of martensite. However, the annealing at 650 °C led to partial reversion of martensite, the modifications were associated with austenite regions that did not transform into α' -martensite, or regions formed by austenite from the reversal of α' -martensite⁵¹. Both studies reported that these structural modifications tend to expand as the deformation rate increases^{47,51}. The most deformed structure of the CR sample showed greater evidence of these microstructural changes compared with the CRH sample. Therefore, the emphasized regions inside the austenite grains gained a greater anodic potential and are revealed with Beraha etchant. These characteristics cannot only be attributed to martensite laths but could be some austenitic regions that did not transform into martensite that was induced by deformation.

Isothermal annealing was responsible for significant microstructural changes in DSS due to recovery and recrystallization. The two phases of DSS during annealing treatment show different softening behavior, while ferrite shows predominantly recovery-type behavior, austenite shows discontinuous recrystallization^{52,53}.

A higher volume fraction of austenite than ferrite is observed for the FP1 sample, the fact seemed to be associated with the reversion mechanism from deformation-induced α' -martensite to austenite. Microstructural changes inside the austenitic lamellae are related to austenite-ferrite transformation¹⁶. Recrystallization of the ferrite progressed during annealing at 1000 °C so that the ferrite lamellae became larger. Further increasing the annealing temperature to 1100 °C promoted a microstructural transition to austenite islands formed from the ferritic matrix.

However, annealing at 900 °C for the FP1H led to the retention of the CRH structure. Upon increasing the annealing temperature, the growth of ferrite subgrains is restricted along the ND but occurs laterally along the RD⁵². According to Ahmed et al.⁵² this ensures that the subgrains are separated by low angle boundary after they mutually impinge, resulting in the bamboo-type morphology in ferrite. In the case of the bamboo type morphology in austenite, the perpendicular boundaries are the high angle grain boundaries. The result is a bamboo-structure for each phase, where the grain boundaries ran perpendicular to the phase boundaries, and the grains extended through the full height of the respective layers⁵³.

The increasing annealing temperature promoted a transition from the bamboo-like structure to a pearl, a more globular structure. This transformation is controlled by diffusion^{19,45,52,54}. The microstructural transformation process is accelerated with increasing strain hardening, which is supported by the fact that the lamellae thickness of the two phases in the non-homogenized route are finer than the corresponding thickness in the homogenized route. The finer microstructure obtained in the CR sample results in faster diffusion paths and reduced diffusion length, resulting in faster microstructural evolution.

The contrast between the phases is not so pronounced in the SEM images in secondary electron mode, (SEI), so sigma phase identification can be better using the backscattered electron mode, (BEI), as presented in Figure 7. It was used a light etch with Behara etchant that preferentially reveals α phase and emphasizes the γ phase, sigma phase (red circle) presents a lighter color as a consequence of the greater amount of Mo. As the ferrite transforms to σ phase, the surrounding ferrite becomes reduced in Cr and Mo content, with intense pitting formation (black spots – green arrow) after etching.

3.2. Mechanical properties

Figure 8 shows the Vickers microhardness values of the samples. A remarkable microhardness increase was observed after cold rolling. The high hardness achieved at the cold rolled condition is associated with the strain-induced transformation and strain hardening.

After deformation was observed a higher microhardness for the CR sample when compared with the CRH sample. This microhardness result corresponded to an overall increase of 40 pct over the CR sample and 35 pct for the CRH sample.

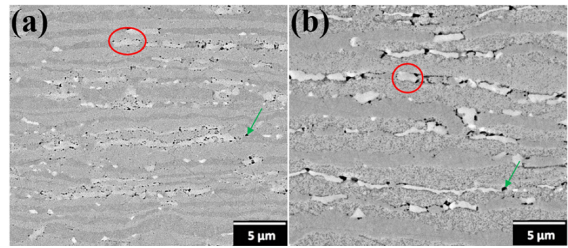


Figure 7. SEM micrographs obtained using BEI of the 2205 DSS annealed at 900 °C for the samples (a) FP1 and (b) for FPH1.

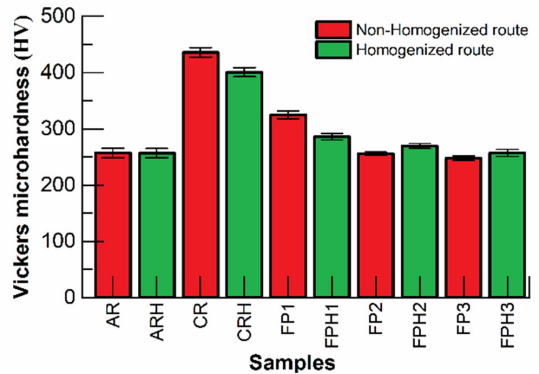


Figure 8. Vickers microhardness of 2205 DSS samples from the non-homogenized route (AR, CR, FP1, FP2, and FP3) and homogenized route (ARH, CRH, FPH1, FPH2, and FPH3).

Thus, although the same amount of thickness reduction, the lower hardness achieved for the CRH sample is associated with lesser strain states and related strain energies.

After the annealing treatment of the cold rolled samples, a substantial decrease in microhardness is observed. The softening mechanism was promoted by recovery and recrystallization phenomena and the reversion of deformation-induced α' -martensite^{38,39,55,56}. The recrystallization kinetics was reduced with the homogenization step, for this reason, the hardness of the samples annealed is slightly lower.

The lowest annealing temperature among the annealed samples showed the greatest microhardness among annealed samples since at 900 °C precipitation of the sigma phase occurred (Figure 4). The sigma phase has a tetragonal crystallographic structure with 32 atoms per unit cell that increases the hardness due to distortion in the crystal lattice⁵⁷. The higher hardness of the FP1 sample compared with the FPH1 sample indicates the increasing content of the sigma phase and partial recrystallization in the route without homogenization. The result is in agreement as discussed in the microstructural changes.

After annealing at 1000 °C, the increase in annealing temperature did not significantly change the microhardness. The constancy in microhardness was also observed for the AR and ARH samples, despite grain coarsening. Malta et al.⁵⁶ associated this hardness stability with the lack of recrystallization, in which small changes in the microhardness of the completely recrystallized material were observed.

Moura et al.⁵⁸ studies indicated that after full recrystallization of the ferrite phase, its hardness reaches a constant value.

Regarding the austenite phase, the hardness tends to decrease continuously as the temperature increase since the higher stored energy acts as a driving force for the recrystallization⁵⁸. Malta et al.³⁸ identified the attenuation of the hardness with an increase in the ferrite volume fraction by increasing the annealing temperature. The austenite hardness became more negligible with increasing ferrite volume fraction and consequently annealing temperature^{38,55}.

The engineering stress-strain curves of the 2205 DSS specimens are shown in Figure 9. The yield strength (YS), ultimate tensile strength (UTS), and total elongation (E) of the samples are presented in Table 2. In response to grain coarsening, the ARH sample showed a decrease in the YS and an increase in the E compared to the AR sample. According to Pan et al.⁵⁴, the microstructure uniformity can improve the ductility by increasing the continuity of the ferrite matrix and eliminating the texture effect.

Cold rolling results in a drastic increase in strength at the expense of ductility. After cold rolling the increase in dislocation density from the work hardening process increased the mechanical strength. Several austenite grains are transformed into α' -martensite, which contains high dislocation density. Additionally, ferrite grains were also significantly refined. Dislocation slip is the main mechanism of grain refinement by the dislocation cells and dislocation substructure¹⁸. The homogenization step before cold rolling

slightly decreases YS and UTS and increases E for the CRH sample compared to the CR sample.

It is observed that the tensile flow of the 2205 DSS was influenced by the stress relief annealing process. Samples annealed at 900 °C obtained partial ductility recovery with the highest increase YS and UTS among the annealed samples. At this temperate precipitation of the brittle sigma phase occurred (Figure 1). σ precipitation occurs predominantly at grain boundaries in the alloy and can lead to a higher strain strength and lower ductility⁵⁹.

Further increase in annealing temperature enhances recovery and recrystallization, increasing the ductility. The decrease in tensile properties observed after annealing at temperatures above 1000 °C can be attributed to the increased ferrite volume fraction.

3.3. Passive properties

Figure 10 shows typical potentiodynamic polarization curves of the samples in a borate buffer solution at room temperature. According to this, the samples show the same curve shapes, where the current changes smoothly and linearly around the corrosion potential, manifesting anodic Tafel behavior. The breakdown potentials of the samples are similar in borate buffer solution.

Figure 10 Potentiodynamic polarization curves in borate buffer solution for 2205 DSS (a) AR, CR, FP1, FP2, and FP3 samples, (b) ARH, CRH, FPH1, FPH2, and FPH3.

However, it is observed slightly changes in the current density among the samples in the low passive region ($< 0.4 V_{Ag/AgCl}$), this implies different rates of dissolution of the passive film, however, no clear trend was observed. After the potential of $0.4 V_{Ag/AgCl}$, it is worthwhile to note that no significant changes occurred in the passive current densities.

Mott-Schottky technique was performed for investigating the semi-conductivities and charge carrier densities of passive film formed on 2205 DSS through thermomechanical processing. According to the Mott-Schottky theory, the space charge capacitances of n-type and p-type semiconductor are given by Equation 1⁵:

$$C^{-2} = C_H^{-2} + C_{SC}^{-2} = \pm \frac{2}{eN\epsilon_s\epsilon_0} \left(E - E_{fb} - \frac{kT}{e} \right) \quad (1)$$

Table 2. Tensile Test Results of 2205 DSS.

Sample	YS (MPa)	UTS (MPa)	E (%)
AR	596 ± 4	767 ± 1	44 ± 1.2
CR	1362 ± 21	915 ± 14	4 ± 0.1
FP1	783 ± 26	1040 ± 14	16 ± 2.4
FP2	568 ± 6	799 ± 12	37 ± 0.5
FP3	553 ± 9	785 ± 3	36 ± 1.3
ARH	505 ± 10	724 ± 5	47 ± 1.7
CRH	1261 ± 24	1295 ± 21	4 ± 0.1
FPH1	636 ± 13	879 ± 30	21 ± 2.5
FPH2	537 ± 9	776 ± 6	42 ± 1.8
FPH3	515 ± 20	744 ± 16	39 ± 1.4

YS, yield strength (offset 0.2 pct); UTS, ultimate tensile strength; E, total elongation.

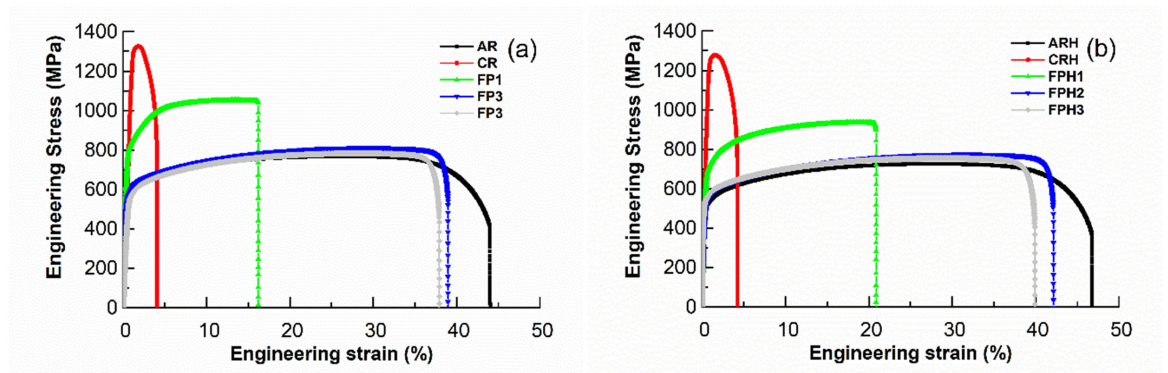


Figure 9. Engineering stress–strain curves of the 2205 DSS samples (a) AR, CR, FP1, FP2, and FP3 samples, (b) ARH, CRH, FPH1, FPH2, and FPH3.

where C_H and C_{SC} are the Helmholtz capacitance and the space charge capacitance, respectively. N is the charge carrier density (the donor density for n-type (N_D) or the acceptor density for p-type (N_A) semiconductors), e is the electron charge (1.6×10^{-19} C), ϵ_0 is the vacuum permittivity (8.854×10^{-14} F cm $^{-1}$), ϵ_s is the relative dielectric constant of the semiconductor, assumed as 12 for the passive films on stainless steels³, k is the Boltzmann constant (1.38×10^{-23} J K $^{-1}$), T is the absolute temperature, E is the applied electrode potential and E_{fb} is the flat-band potential. The donor and acceptor densities in the passive film can be determined by linear fitting of positive and negative slopes of the linear

zone in Mott-Schottky plots. The capacitance value was calculated by Equation 2¹⁷:

$$C = (-Z_{im} 2\pi f)^{-1} \quad (2)$$

where Z_{im} is the imaginary part of the impedance and f is the frequency. The 1000 Hz is used in this study.

Figure 11a,b shows the Mott-Schottky plots of the passive films formed on 2205 DSS samples after thermomechanical processing in borate buffer solution. A positive slope in this plot indicates an n-type charge carrier behavior, whereas the opposite reflects a p-type semi-conductor. The Mott-Schottky

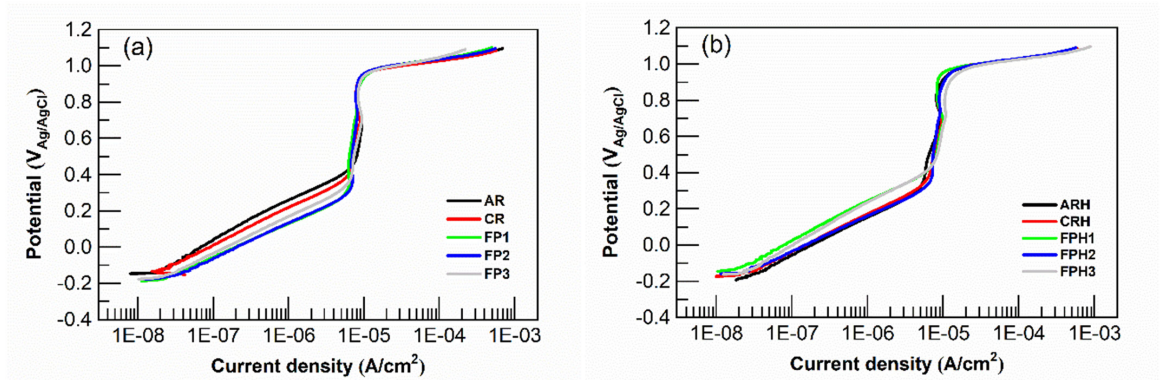


Figure 10. Potentiodynamic polarization curves in borate buffer solution for 2205 DSS (a) AR, CR, FP1, FP2, and FP3 samples, (b) ARH, CRH, FPH1, FPH2, and FPH3.

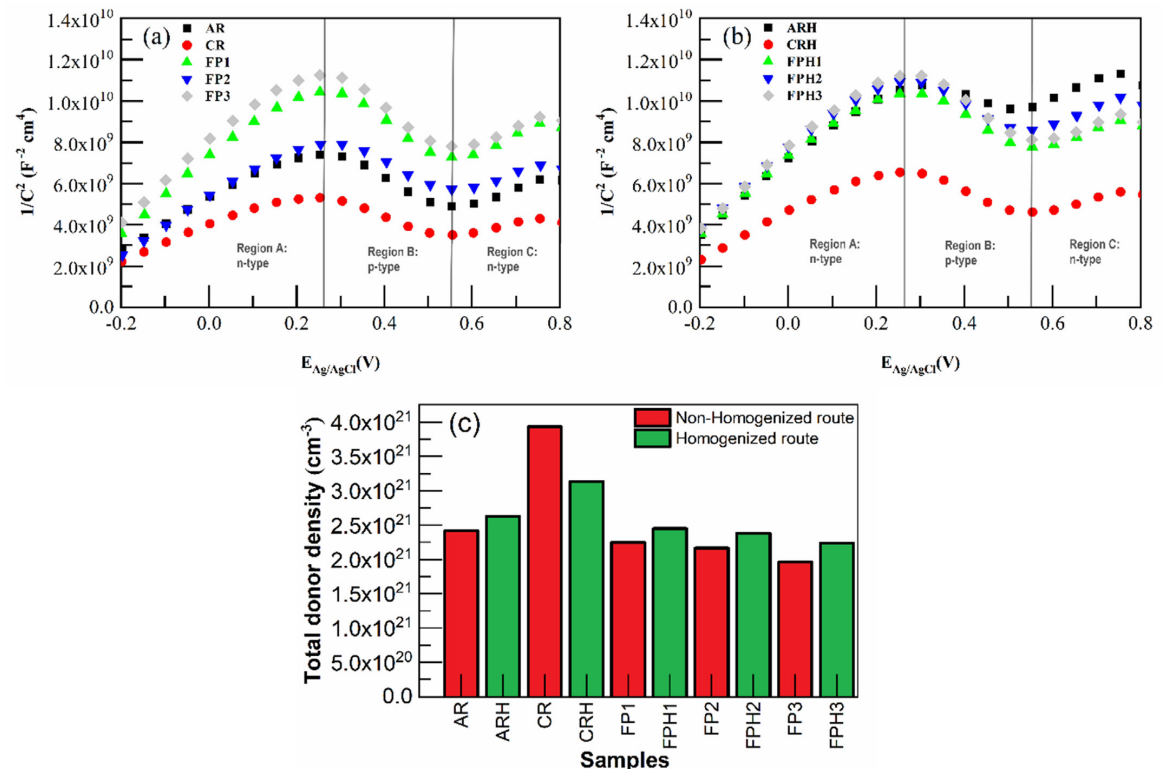


Figure 11. Mott-Schottky plots for passive films formed on 2205 DSS samples from the from (a) nonhomogenized route (AR, CR, FP1, FP2, and FP3), (b) homogenized route (ARH, CRH, FPH1, FPH2, and FPH3), (c) the effect of the thermomechanical processing on the total donor concentrations in the passive film.

analysis reveals that the passive film formed on both routes exhibits n-type and p-type semiconducting characteristics irrespective of the thermomechanical processing.

As depicted in Figure 11a,b, the charge carrier property of the passive film on 2005 DSS indicates a similar semiconductor behavior with three different regions. Two slopes in passive films formed 2205 DSS are generally attributed to two different semiconducting layers, indicating that the passive films are formed as one inner layer rich in chromium oxide and an outer layer rich in iron oxides^{18,60-62}.

In Figure 11a,b, the first region (region A), which has a positive slope, the passive film (barrier layer) displays n-type semi-conductivity, this semiconductor behavior is characteristic of Fe₂O₃⁶³. According to Yao et al.³, the composition of the barrier layer in region A is $\gamma\text{-Fe}_{2+x}\text{O}_{3-y}$ which mainly contributes to the n-type semiconductor property.

Between 0.25 V_{Ag/AgCl} and 0.55 V_{Ag/AgCl} (region B), the p-type behavior of the passive film is probably due to the generation of cation vacancies (electronic acceptors and p-type dopants) at the passive film/solution interface, such that these species become dominant⁶⁴. Besides, according to Yao et al.³ the primary composition of the outer surface of the barrier layer passive film changes from iron-rich oxide to chromium-rich oxide/hydroxide and this can also result in p-type semiconductor property.

In the region C, at potentials more positive than 0.55 V_{Ag/AgCl} the positive slope is characteristic of an n-type semiconductor. According to Luo et al.⁶⁰, this change in the slope of C⁻² vs. E started from 0.55 V_{Ag/AgCl} and can be interpreted in terms of the capacitive contribution of a secondary external layer, most probably the iron oxyhydroxide layer FeOOH, and would continue to be oxidized into Fe₂O₃ in the presence of oxygen. The existence of the second positive slope in Figure 11a,b could be attributed to a deep donor level in the bandgap, which indicates that the capacitance behavior of the oxide films formed on DSS is supported by a band structure model of a semiconductor electrode containing multiple donor levels or associated with the presence of Fe²⁺ ions in the tetrahedral and octahedral positions, respectively^{18,60,61,63}.

Based on the polarization curves shown in Figure 10, the passive behavior is established in the Region B of Mott–Schottky plots, indicating that the transition of the active-passive behavior is related to changes from iron-rich oxide to chromium-rich oxide/hydroxide in the barrier layer. It is seen that the passive region possesses a turning point with a slight increase in current density of about 0.55 V_{Ag/AgCl}. According to Luo et al.⁶⁰, transpassive oxidation does not seem to lead to the dissolution of the passive film, but the film is transformed from Fe-rich primary oxide film to a Fe-rich secondary oxide film. At potential over 0.75 V_{Ag/AgCl} there is a slight decrease in current density. Here, the change seems to be related to changes from the Fe-rich secondary oxide film to a Cr-rich oxide stabilizing the passive film and preventing the oxide layer from breaking down.

According to Equation 1, the donor densities have been determined from the positive slopes of Mott-Schottky plots. N_{D1} and N_{D2} are shallow and deep donor levels, respectively¹⁸. According to Equation 3⁵, the positive slopes of the linear portion of the C⁻² vs. applied potential (E) give the charge carrier density N, from the relation:

$$N = \frac{2}{m e \epsilon_s \epsilon_0} \quad (3)$$

where m is the slope of the Mott–Schottky plot in the linear-region of interest. The total donor density (N_{D1} and N_{D2}) values could be estimated from the slope of the straight lines of C⁻² vs. E. Figure 11c shows the calculated donors ($N_{D1} + N_{D2}$) for the passive films formed on 2205 DSS in borate buffer solution. The orders of magnitude are around 10²¹ cm⁻³ and are comparable to those reported for other stainless steels in borate solution^{3,18,27,62}.

PDM (point defect model)⁶⁵ predicted that the cation vacancies are generated at the film/solution interface, while cation interstitials and oxygen vacancies are generated at the metal/film interface. The formation, annihilation, and transport of point defects in the passive film result in their growth and breakdown^{3,50,61,65,66}. PDM explains that the more oxygen vacancies, the greater the donor concentration in the oxide film, the more easily the oxide film is destroyed⁶⁷. Therefore, a higher value of donor concentration in the passive film was associated with the weakest passive film.

Figure 11c shows that grain coarsening, promoted by the homogenization step before cold rolling (Figure 4b, 5b), led to a higher total donor density for the ARH sample than the for the AR sample. Similar results were obtained by Mondal et al.¹³ for super duplex stainless steel, who reported that after solution annealing, the grain coarsening of the ferrite phase increased the defect density and reduced the corrosion performance and stability of the oxide film. On the other hand, the austenite phase showed a balance between grain coarsening and substrate Mo content, manifesting a non-monoatomic behavior.

The total donor concentration in the passive film increased significantly after cold rolling. Studies have reported the increase in donor density with an increase in the cold deformation level and stated that high donor density is harmful to the stability of the passive film^{50,68}. Therefore, the Nd is higher for the CR sample than the CRH sample due to the higher dislocation density. According to Jinlong et al.⁵⁰, more dislocations induce more oxygen vacancies in the passive film and decrease its compactness and corrosion resistance. After annealing, the dislocation density decreases and, consequently, it is observed a decrease in Nd of the annealed samples.

According to Figure 11c, after annealing at 900 °C, 1000 °C, and 1100 °C, the donor densities of the passive film formed on the non-homogenized route were lesser than that of the homogenized route which reflected better passivation behavior samples without the homogenization step. In other words, the homogenization step before cold rolling increased the number of point defects in the passive film formed of the annealed samples. This could be related to the higher grain refinement of the FP1, FP2, and FP3 samples (Figure 5c, g, i, respectively) and the formation of a stable passive film. Numerous studies have related grain refinement after annealing with a decrease in donor densities^{13,18,66}. According to Mondal et al.¹³ three different models have been proposed to explain the beneficial aspects of grain size refinement: (i) conversion of Cr(OH)₃ to Cr₂O₃, (ii) higher boundary density promoting Cr diffusion (bulk to surface)

and formation of Cr_2O_3 film and (iii) lower defect density enhancing film stability. Moreover, Jinlong et al.¹⁸ showed that the grain refinement promoted the enrichment of Cr_2O_3 and Fe_2O_3 and inhibited $\text{Cr}(\text{OH})_3$ and FeO , which could significantly improve the corrosion resistance of 2205 DSS.

The electrochemical properties of the film on the surface of the stainless steel were measured using electrochemical impedance spectroscopy (EIS) and are shown in Figure 12. In Figure 12a,c, the real impedance is plotted vs. the imaginary impedance and it is seen that the Nyquist diagrams exhibit a depressed semicircle with a capacitive arc. A remarkable decrease in the diameter of the Nyquist plot is observed after cold rolling. Theoretically, the diameter of the capacitive loop is associated with the charge transfer resistance, and a larger semicircle arc diameter indicates a higher corrosion resistance of the film⁶⁹.

The semicircle of the Nyquist plot is the smallest for the CR sample, implying reduced corrosion resistance of the passive film. Bode plots are also presented in Figure 12b,d and show only one time constant and high phase angle values over a wide frequency range reviling the formation and growth of a passive film⁶⁶.

The equivalent circuit in Figure 13 is proposed for fitting it to EIS data and thereby quantifying the electrochemical parameters, in which R_s is the solution resistance, CPE is the constant phase angle element, and R_{ct} is the charge transfer resistance. Based on the equivalent circuit, the EIS data were fitted by Zview software and the results are listed in Table 3.

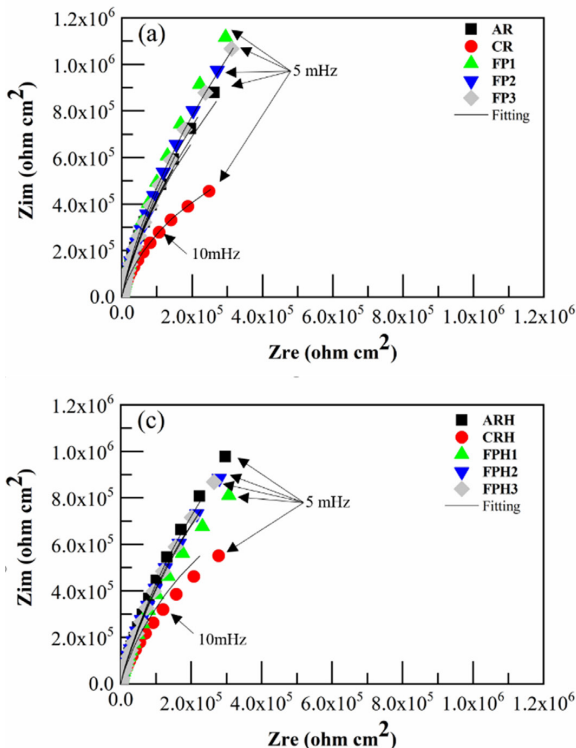


Figure 12. Nyquist plots (a,c) and (b,d) Bode phase plots of passive films formed in borate buffer solution for 2205 DSS (a, b) AR, CR, FP1, FP2, and FP3 samples and (c,d) ARH, CRH, FPH1, FPH2, and FPH3 samples.

If the impedance response of the constant-phase element (CPE) can be correlated with an effective capacitance, the film thickness may be obtained from the Equation 4^{70,71}:

$$C_{eff} = \frac{\epsilon \epsilon_0}{\delta} \quad (4)$$

where C_{eff} is the effective capacitance of the passive film, δ is the film thickness, ϵ (~ 12) is the dielectric constant, and ϵ_0 is the permittivity of vacuum with a value (8.854×10^{-14} Fcm^{-1}). An expression for the C_{eff} is given by Equation 5^{70,71}:

$$C_{eff, PL} = gQ(\rho_\delta \epsilon \epsilon_0)^{1-n} \quad (5)$$

where Q is the constant representative of the CPE and n is the exponent of the CPE (Table 3), ρ_δ is the resistivity. Also, the parameter ρ_δ is equal to $\rho_\delta = 500 \Omega \text{ cm}$ and g is a function of n which can be expressed by Equation 6^{70,71}:

$$g = 1 + 2.88(1-n)^{2.375} \quad (6)$$

The charge transfer resistance (R_{ct}) and the thickness of passive films (δ) on 2205 DSS are shown in Figure 14a,b.

It is observed that the R_{ct} of the AR sample is similar that of the ARH sample, considering the deviation, and the same tendency is observed for δ (Figure 14b). As can be seen, after cold rolling, there was a remarkable decrease in R_{ct} however, no difference between the film thicknesses was observed. Luo et al.⁶⁸ reported that cold deformation modifies the grain size and leads to a phase transformation from the austenite

phase to the martensite phase. Furthermore, it modifies the composition of the passive film at room temperature and the results show a less protective ability of the passive film with an increase in deformation level of 2205 DSS duplex stainless steel in simulated concrete pore solution. Gao et al.³⁷ studied 2205 DSS in a 3.5% NaCl solution and the results indicate that σ phase, strain-induced martensite, as well as the defects, induced by cold deformation, lower the corrosion resistance.

After annealing, R_{ct} increases due to a lower dislocation density. The samples from the non-homogenized route presented higher R_{ct} compared to the homogenized route, due to grain refinement from the recrystallized microstructure and a higher amount of reverted austenite from the martensite-austenite

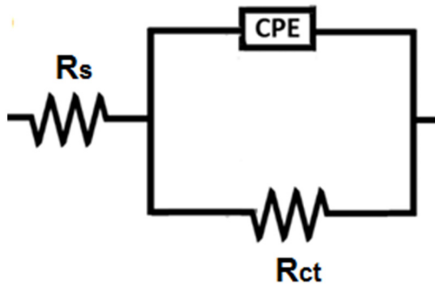


Figure 13. The electrochemical equivalent circuit for EIS fitting.

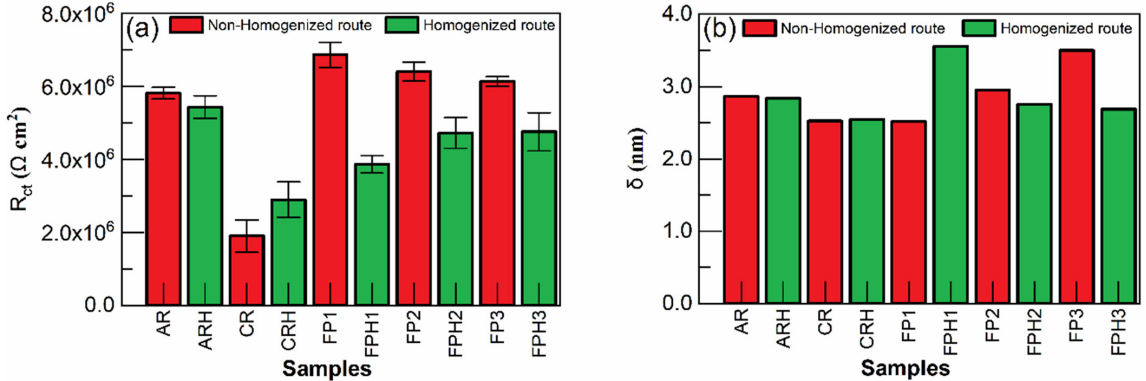


Figure 14. Correlation between non-homogenized route (AR, CR, FP1, FP2, and FP3) and homogenized route (ARH, CRH, FPH1, FPH2, and FPH3) on (a) charge transfer resistance of passive film and (b) the thickness of the passive film for the 2205 DSS thermomechanical treated.

Table 3. Electrochemical parameters fitted with an equivalent circuit based on EIS spectra of the 2205 DSS samples in a borate buffer solution.

Sample	R_s ($\Omega \text{ cm}^2$)		R_{ct} ($\Omega \text{ cm}^2$)		Q ($\Omega^{-1} \text{ cm}^{-2} \text{ s}^n$)		n		χ^2	
	Value	Deviation	Value	Deviation	Value	Deviation	Value	Deviation	Value	Deviation
AR	53.1	1.4	5.82E+06	1.58E+05	2.47E-05	2.53E-06	0.911	0.011	3.1E-3	1.1E-4
CR	60.2	16.9	1.90E+06	5.42E+05	3.14E-05	9.72E-06	0.905	0.010	4.3E-3	1.2E-5
FP1	63.4	6.1	6.87E+06	3.44E+05	2.52E-05	5.31E-06	0.916	0.006	2.6E-3	7.1E-5
FP2	61.4	4.6	6.41E+06	3.00E+05	2.82E-05	4.20E-06	0.903	0.010	4.2E-3	1.8E-4
FP3	59.8	6.0	6.14E+06	1.32E+05	2.57E-05	8.20E-06	0.899	0.004	4.7E-3	9.6E-4
ARH	61.0	3.5	5.44E+06	4.86E+05	2.35E-05	2.61E-06	0.913	0.023	2.1E-3	2.6E-4
CRH	50.7	10.2	2.90E+06	7.84E+05	2.85E-05	4.44E-06	0.905	0.006	7.6E-3	4.5E-4
FPH1	87.4	2.3	3.87E+06	2.44E+05	2.38E-05	1.54E-06	0.902	0.006	3.6E-3	2.2E-4
FPH2	59.1	7.1	4.73E+06	5.18E+05	2.64E-05	3.97E-06	0.909	0.013	1.8E-3	1.6E-5
FPH3	62.5	3.0	4.76E+06	6.25E+05	2.36E-05	1.82E-06	0.915	0.003	3.3E-3	1.5E-4

transformation. The increase in annealing temperature from 900 °C to 1100 °C decreases the corrosion resistance in this case. According to Zhang et al.¹², the increasing annealing temperatures increased the ferrite content and diluted the key alloying elements in the ferrite, lowering the corrosion resistance. However, it can be noticed in Figure 14b an increase in δ increasing annealing temperature for FP1, FP2, and FP3 samples indicating a formation of a thicker passive film.

However, the samples from the homogenized route presented an opposite behavior. As can be seen in Figure 5e, the sample FP1 presented a recrystallized microstructure and the FPH1 did not show phase recrystallization. Figure 14a shows that the corrosion resistance of the FPH1 passive film is higher than that of the CRH sample but lower than that of the FPH2 and FPH3 samples. Therefore, annealing to 1000 °C led to recrystallization of the austenite phase and increased R_{ct} , a further increase in annealing temperature to 1100 °C did not change the R_{ct} . It is observed in Figure 14b that for the homogenized route that the passive film thickness decreases from 900 °C to 1000 °C annealing temperature and could be related to austenitic recrystallization, leading to the formation of a passive film less thick but denser.

Although annealing at 900 °C after cold rolling led to the formation of the sigma phase, the amount of secondary phase seems to have little or no influence on the decrease in corrosion resistance of the passive film of 2205 DSS in

the non-homogenized route. A higher R_{ct} was obtained at this annealing temperature. Man et al.⁷² confirmed that the reversed austenite had a beneficial effect on the intergranular corrosion of martensitic stainless steel due to the formation of reversed austenite at the Cr-depleted regions. Besides, this temperature allows bulk chromium diffusion in the passive film. The lower R_{ct} for FPH1 samples is more related to the absence of recrystallization and less reversed austenite due to low stored energy after cold rolling than the presence of the σ phase.

The EIS results indicate that the recrystallization of ferrite and austenitic phase and consequently grain refining increases the corrosion resistance of the 2205 DSS in borate buffer solution. However, the grain growth of the ferrite phase (Figure 5e,j) could decrease the corrosion resistance. These EIS results are in agreement with the Mott-Schottky analysis.

Figure 15 shows the XPS O 1s, Fe 2p_{3/2}, Cr 2p_{3/2}, Ni 2p_{3/2}, Mo 3d and N 1s spectra obtained for the passive film at 0.6 mV_{Ag/AgCl} for 2h on the 2205 DSS. In addition, according to the quantitative analysis of the passive film, the cationic fraction of the elements was calculated by Equation 7⁷³:

$$C_x = \frac{I_x / S_x}{\sum I_i / S_i} \quad (7)$$

where C_x is the atomic percentage, I_x is the peak intensity corresponding to the area of the element M, and S_x is the sensitivity factor based on the XPS instrument. In this study, the sensitivity factors of Cr, Fe, Mo and N are 11.0, 7.82, 9.5 and 1.8, respectively. The binding energies (Eb) related to the spectra deconvolution of the primary compounds and the XPS cationic fraction in the passive film are reported in Table 4.

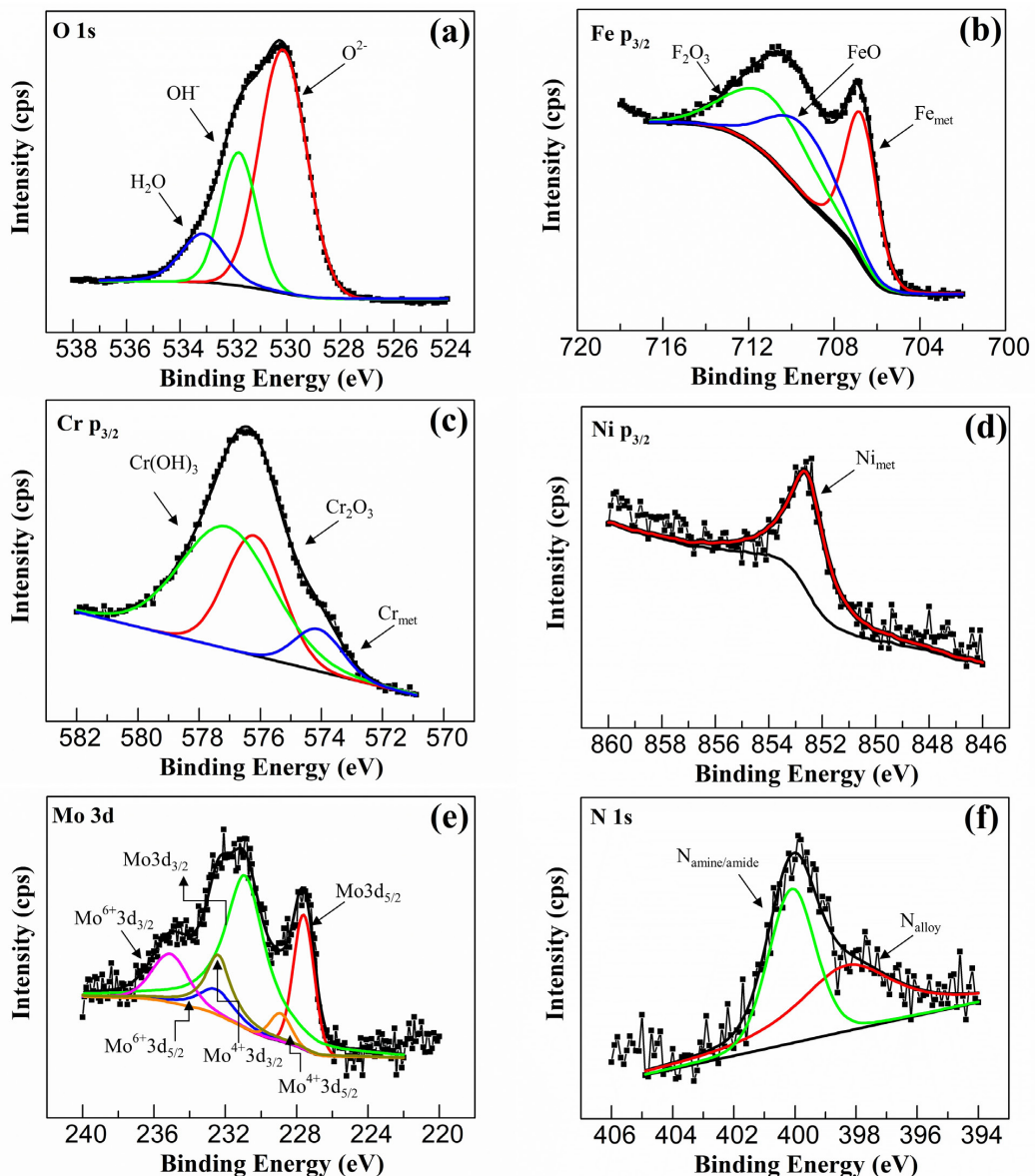


Figure 15. XPS core level spectra recorded for the passive film formed at the surface of the duplex stainless steel (passivation conditions: 0.05 M H₃BO₃ + 0.075 M Na₂B₄O₇·10H₂O, 0.6 V_{Ag/AgCl}, 2 h).

Table 4. The binding energies of the primary compounds obtained from XPS spectra deconvolution and the XPS cationic fraction in the passive film of 2205 duplex stainless steel after passivation at 0.6 VAg/AgCl for 2 h in borate buffer solution.

Element	Peak	Species/binding energy (eV)	Cationic fraction
O	1s	O ²⁻ /530.2; OH ⁻ /531.9; H ₂ O/533.2	-
Fe	2p _{3/2}	Fe _{met} ⁰ /706.7; Fe ₂ O ₃ /710.9.2; FeO/709.4	Fe ₂ O ₃ /0.19; FeO/0.17
Cr	2p _{3/2}	Cr _{met} ⁰ /574.1; Cr ₂ O ₃ /576.2; Cr(OH) ₃ /577.1	Cr ₂ O ₃ /0.24; Cr(OH) ₃ /0.37
Ni	2p _{3/2}	Ni _{met} ⁰ /852.8	-
Mo	3d _{5/2}	Mo _{met} ⁰ /227.8; Mo ⁴⁺ /229.3; Mo ⁶⁺ /232.5	Mo ⁴⁺ /0.008; Mo ⁶⁺ /0.009
	3d _{3/2}	Mo _{met} ⁰ /230.9; Mo ⁴⁺ /232.4; Mo ⁶⁺ /235.6	Mo ⁴⁺ /0.004; Mo ⁶⁺ /0.002
N	1s	N _{alloy} ⁰ /389.3; N _{amine/amide} ⁰ /400.1	N _{amine/amide} ⁰ /0.01

Figure 15a shows the core-level spectra of the passive film formed on 2205 DSS in different regions in the O 1s region, which are primarily O²⁻, OH⁻. The oxygen species in the passive film play the role of bonding metal ions, the main component of the passive film in the solution was O²⁻, which corresponds to the formation of Fe oxides⁵. The primary constituents of the passive film are FeO and Fe₂O₃ (Figure 15b). Similar cationic fraction for FeO and Fe₂O₃ were observed (Table 4), nonetheless, a better corrosion resistance in DSS may be achieved with more iron oxides and fewer ferrous oxides¹⁸.

The Cr 2p_{3/2} spectra (Figure 15c) reveal that there exist three constituent peaks representing metallic state Cr(met), Cr(OH)₃ and Cr₂O₃. According to the cationic fractions in Table 4, the oxide layer of Cr species is mainly composed of Cr(OH)₃. Jinlong et al.⁶¹ results with a 2205 DSS solution annealed and passivated at 0.6 V_{SCE} for 1 h in borate buffer solution shows that the oxide layer of Cr species is mainly composed of Cr₂O₃. Jinlong et al.¹⁸ work with a coarse and ultrafine grained 2205 DSS, indicates that Cr₂O₃ and Fe₂O₃ enhance the corrosion resistance of the passive film in borate buffer solution and that the low protective Cr(OH)₃ weaker the passive film.

Figure 15d indicates that no oxidized nickel is detected. Luo et al.⁶⁸ study indicates that the Mo species in the passive film of a 2205 DSS cold rolled in a simulated concrete pore solution slightly change with cold deformation. A contribution corresponding to nitrogen present in the alloy is detected (Figure 15f). This corresponding to (N_{allow}) nitrogen present in the alloy either dissolved in solid solution in the metal or segregated as nitride, and nitrogen in amine and/or amide groups arising from the surface contamination⁴. The metal nitride formation is harmful to the corrosion resistance of the DSS film⁶⁸.

4. Conclusions

In this study, the influence of the homogenization step before cold rolling and subsequent annealing at 900 °C, 1000 °C, and 1100 °C on the microstructure and corrosion resistance of the passive film on the DSS 2205 was investigated by metallographic, mechanical, and electrochemical analyses. The primary conclusions are as follows:

1. The band-like morphology of the as-received specimen coarsened with homogenization was replaced by a pancake structure after cold rolling. Cold rolling promoted a reduction in the phase

spacing accompanied by increasing in dislocation density and stored energy and led to the α'-martensite formation. The homogenization step before cold rolling decreases strain hardening and reduced recrystallization kinetics.

2. Microhardness remarkably increases with cold rolling. After annealing microhardness decreases due to a softening mechanism promoted by recovery and recrystallization phenomena and the reversion of deformation-induced α'-martensite. Tensile tests showed that the homogenization step increases ductility. Cold rolling results in a drastic increase in strength at the expense of ductility. Further increase in annealing temperature enhance recovery and recrystallization increasing plasticity.
3. Mott-Schottky analysis indicated that the passive films behave as n-type and p-type semiconductors. The changes in the phase proportion on the microstructure and redistribution of alloying elements caused by thermomechanical did not change the semiconductor type of the passive films. Also, this analysis indicated that the total donor densities are around 10²¹ cm⁻³ and increased after cold rolling and decreased after annealing. The total donor densities of the annealed samples were lower in the non-homogenized route owing to higher grain refinement.
4. EIS measurements indicate that grain coarsening promoted by homogenization decreases the passive film corrosion resistance. Cold rolling significantly decreased the corrosion resistance. The homogenized cold rolled sample had a higher corrosion resistance than the non-homogenized cold rolled sample due to a lesser dislocation density. Annealing after cold rolling increases corrosion resistance. The homogenized step before cold rolling lowers the stored energy of the cold rolled sample and slower the recrystallization kinetics, decreasing corrosion resistance when compared to non-homogenized annealed samples.
5. XPS analysis of the passive film formed in borate buffer solution at the middle of the passive region indicated that the passive film of the sample cold rolled after homogenization was possibly weaker due to a high amount of Cr(OH)₃ and FeO.

5. Acknowledgments

The authors are grateful to Aperam South America for the steel samples supply. Also thank the CAPES-PPGEM/UFMG-REDEMAT/UFOP, CNPq and FAPEMIG for the student fellowship and financial support. The authors express their gratitude to Prof. Herman S. Mansur from the Center of Nanoscience, Nanotechnology and Innovation – CeNano²/CEMUCASI/UFMG for the XPS analysis

6. References

- Gunn R. Duplex stainless steel: microstructure, properties and applications. 3rd ed. Cambridge: Abington Publishing; 2003.
- Alvarez-Armas I, Degallaix-Moreuil S. Duplex stainless steels. 1st ed. Cambridge: Wiley-ISTE; 2009.
- Yao J, MacDonald DD, Dong C. Passive film on 2205 duplex stainless steel studied by photo-electrochemistry and ARXPS methods. *Corros Sci*. 2019;146:221-32. <http://dx.doi.org/10.1016/j.corsci.2018.10.020>.
- Gardin E, Zanna S, Seyeux A, Allion-Maurer A, Marcus P. Comparative study of the surface oxide films on lean duplex and corresponding single phase stainless steels by XPS and ToF-SIMS. *Corros Sci*. 2018;143:403-13. <http://dx.doi.org/10.1016/j.corsci.2018.08.009>.
- Gardin E, Zanna S, Seyeux A, Allion-Maurer A, Marcus P. XPS and ToF-SIMS characterization of the surface oxides on lean duplex stainless steel: global and local approaches. *Corros Sci*. 2019;155:121-33. <http://dx.doi.org/10.1016/j.corsci.2019.04.039>.
- Tranchida G, Clesi M, Di Franco F, Di Quarto F, Santamaria M. Electronic properties and corrosion resistance of passive films on austenitic and duplex stainless steels. *Electrochim Acta*. 2018;273:412-23. <http://dx.doi.org/10.1016/j.electacta.2018.04.058>.
- Lin DY, Liu YF, Chen CH, Chen YC, Huang WP, Yang SM, et al. The effect of annealing temperature on the corrosion behavior of silver alloyed 2205 duplex stainless steel. *Int J Mater Res*. 2014;105(3):258-64. <http://dx.doi.org/10.3139/146.111021>.
- Zhang X, Tang J, Liu H, Gong J. Effects of pre-strain on sensitization and intergranular corrosion for 304 stainless steel. *Eng Fail Anal*. 2019;106:104179. <http://dx.doi.org/10.1016/j.engfailanal.2019.104179>.
- Tan H, Wang Z, Jiang Y, Han D, Hong J, Chen L, et al. Annealing temperature effect on the pitting corrosion resistance of plasma arc welded joints of duplex stainless steel UNS S32304 in 1.0M NaCl. *Corros Sci*. 2011;53(6):2191-200. <http://dx.doi.org/10.1016/j.corsci.2011.02.041>.
- Yang Y, Tan H, Zhang Z, Wang Z, Jiang Y, Jiang L, et al. Effect of annealing temperature on the pitting corrosion behavior of UNS S82441 duplex stainless steel. *Corrosion*. 2013;69(2):167-73. <http://dx.doi.org/10.5006/0717>.
- Tan H, Jiang Y, Deng B, Sun T, Xu J, Li J. Effect of annealing temperature on the pitting corrosion resistance of super duplex stainless steel UNS S32750. *Mater Charact*. 2009;60(9):1049-54. <http://dx.doi.org/10.1016/j.matchar.2009.04.009>.
- Zhang J, Hu X, Lin P, Chou K. Effect of solution annealing on the microstructure evolution and corrosion behavior of 2205 duplex stainless steel. *Mater Corros*. 2019;70(4):676-87. <http://dx.doi.org/10.1002/maco.201810536>.
- Mondal R, Rajagopal A, Bonagani SK, Prakash A, Fuloria D, Sivaprasad PV, et al. Solution annealing of super duplex stainless steel: correlating corrosion performance with grain size and phase-specific chemistry. *Metall Mater Trans, A Phys Metall Mater Sci*. 2020;51(5):2480-94. <http://dx.doi.org/10.1007/s11661-020-05672-w>.
- Cho HS, Lee K. Effect of cold working and isothermal aging on the precipitation of sigma phase in 2205 duplex stainless steel. *Mater Charact*. 2013;75:29-34. <http://dx.doi.org/10.1016/j.matchar.2012.10.006>.
- Chan KW, Tjong SC. Effect of secondary phase precipitation on the corrosion behavior of duplex stainless steels. *Materials*. 2014;7(7):5268-304. <http://dx.doi.org/10.3390/ma7075268>.
- Rezende SC, Cronemberger MER, Silva R, Rovere CAD, Kuri SE, de Sousa LL, et al. Effect of solution annealing time on the microstructure and corrosion resistance of duplex stainless steel. *Mater Sci Forum*. 2018;930:374-9. <http://dx.doi.org/10.4028/www.scientific.net/MSF.930.374>.
- Badji R, Bouabdallah M, Bacroix B, Kahloun C, Belkessa B, Maza H. Phase transformation and mechanical behavior in annealed 2205 duplex stainless steel welds. *Mater Charact*. 2008;59(4):447-53. <http://dx.doi.org/10.1016/j.matchar.2007.03.004>.
- Jinlong L, Tongxiang L, Chen W, Limin D. Comparison of corrosion properties of passive films formed on coarse grained and ultrafine grained AISI 2205 duplex stainless steels. *J Electroanal Chem*. 2015;757:263-9. <http://dx.doi.org/10.1016/j.jelechem.2015.09.036>.
- Malta PO, Dias FL, de Souza ACM, Santos DB. Microstructure and texture evolution of duplex stainless steels with different molybdenum contents. *Mater Charact*. 2018;142:406-21. <http://dx.doi.org/10.1016/j.matchar.2018.06.006>.
- Dias FL, Cardeal Stumpf G, Ferreira de Dafé SS, Santos DB. Homogenisation effect on mechanical and pitting behaviour of 2205 Duplex Stainless Steel. *Mater Sci Technol*. 2020;36(16):1796-804. <http://dx.doi.org/10.1080/02670836.2020.1836738>.
- Gennari C, Lago M, Bögre B, Meszaros I, Calliari I, Pezzato L. Microstructural and corrosion properties of cold rolled laser welded UNS S32750 duplex stainless steel. *Metals*. 2018;8(12):1-17. <http://dx.doi.org/10.3390/met8121074>.
- Gennari C, Pezzato L, Simonetto E, Gobbo R, Forzan M, Calliari I. Investigation of electroplastic effect on four grades of duplex stainless steels. *Materials*. 2019;12(12):1-18. <http://dx.doi.org/10.3390/ma12121911>.
- Pezzato L, Lago M, Brunelli K, Breda M, Calliari I. Effect of the heat treatment on the corrosion resistance of duplex stainless steels. *J Mater Eng Perform*. 2018;27(8):1-10. <http://dx.doi.org/10.1007/s11665-018-3408-5>.
- Malta PO, Condé BL, Assumpção RF, Perasoli DB, Sicupira DC, Santos DB. Effect of annealing temperature on mechanical behavior, pitting resistance and grain boundary character of a 2304 lean duplex stainless steel. *Metall Mater Trans, A Phys Metall Mater Sci*. 2019;50(6):2665-77. <http://dx.doi.org/10.1007/s11661-019-05193-1>.
- Knutsson A, Hedstrom P, Oden M. Reverse martensitic transformation and resulting microstructure in a cold rolled metastable austenitic stainless steel. *Mater Technol Reverse*. 2008;79(6):433-9. <http://dx.doi.org/10.1002/srin.200806149>.
- Dickson MJ. The significance of texture parameters in phase analysis by X-ray diffraction. *J Appl Cryst*. 1969;2(4):176-80. <http://dx.doi.org/10.1107/S0021889869006881>.
- Hongyun L, Yubo Z, Hongdou L, Jinlong L, Yue M. Characterization of the oxide films formed on low temperature sensitized AISI 321 stainless steel with different strain levels in elevated temperature borate buffer solution. *J Alloys Compd*. 2017;696:1235-43. <http://dx.doi.org/10.1016/j.jallcom.2016.12.107>.
- Ge HH, Xu XM, Zhao L, Song F, Shen J, Zhou GD. Semiconducting behavior of passive film formed on stainless steel in borate buffer solution containing sulfide. *J Appl Electrochem*. 2011;41(5):519-25. <http://dx.doi.org/10.1007/s10800-011-0272-5>.
- Ge HH, Shen J, Song F, Zhao L, Zhou GD. Influence of sulfide on anti-corrosion performance of passive film formed on stainless steel in borate buffer solution. *Adv Mat Res*. 2011;156-157:646-9. <http://dx.doi.org/10.4028/www.scientific.net/AMR.156-157.646>.
- Feng Z, Cheng X, Dong C, Xu L, Li X. Passivity of 316L stainless steel in borate buffer solution studied by Mott-Schottky

- analysis, atomic absorption spectrometry and X-ray photoelectron spectroscopy. *Corros Sci.* 2010;52(11):3646-53. <http://dx.doi.org/10.1016/j.corsci.2010.07.013>.
31. Xu H, Sun D, Yu H. Repassivation behavior of 316L stainless steel in borate buffer solution: kinetics analysis of anodic dissolution and film formation. *Appl Surf Sci.* 2015;357:204-13. <http://dx.doi.org/10.1016/j.apsusc.2015.09.018>.
 32. Xu H, Wang L, Sun D, Yu H. The passive oxide films growth on 316L stainless steel in borate buffer solution measured by real-time spectroscopic ellipsometry. *Appl Surf Sci.* 2015;351:367-73. <http://dx.doi.org/10.1016/j.apsusc.2015.05.165>.
 33. Gonçalves KAMB, Santos DB, Oliveira TR. Analysis of the crystallographic microtexture of a UNS S32205 and a UNS S32304 Duplex stainless steels after cold rolling and heat treatment. *Mater Res.* 2018;21(4). <http://dx.doi.org/10.1590/1980-5373-mr-2017-0873>.
 34. Pinaki PB, Mohammed ZA. Effect of warm-rolling on the formation of microstructure and microtexture of the constituent phases in a duplex Steel. *Mater Sci Forum.* 2014;783-786:2555-60. <http://dx.doi.org/10.4028/www.scientific.net/MSF.783-786.2555>.
 35. Luo H, Wang X, Dong C, Xiao K, Li X. Effect of cold deformation on the corrosion behaviour of UNS S31803 duplex stainless steel in simulated concrete pore solution. *Corros Sci.* 2017;124:178-92. <http://dx.doi.org/10.1016/j.corsci.2017.05.021>.
 36. Tavares SSM, Pardal JM, Silva MR, Oliveira CAS. Martensitic transformation induced by cold deformation of lean duplex stainless steel uns S32304. *Mater Res.* 2014;17(2):381-5. <http://dx.doi.org/10.1590/S1516-14392013005000157>.
 37. Gao T, Wang J, Sun Q, Han P. Corrosion behavior difference in initial period for hot-rolled and cold-rolled 2205 duplex stainless steels. *Metals.* 2018;8(6):407. <http://dx.doi.org/10.3390/met8060407>.
 38. Malta PO, Condé BL, Assumpção RF, Perasoli DB, Sicupira DC, Santos DB. Effect of annealing temperature on mechanical behavior, pitting resistance and grain boundary character of a 2304 lean duplex stainless steel. *Metall Mater Trans, A Phys Metall Mater Sci.* 2019;50(6):2665-77. <http://dx.doi.org/10.1007/s11661-019-05193-1>.
 39. Moallemi M, Zarei-Hanzaki A, Baghbadorani HS. Evolution of microstructure and mechanical properties in a cold deformed nitrogen bearing TRIP-assisted duplex stainless steel after reversion annealing. *Mater Sci Eng A.* 2017;683:83-9. <http://dx.doi.org/10.1016/j.msea.2016.10.105>.
 40. Pramanik S, Bera S, Ghosh SK. Influence of cold rolling on microstructural evolution in 2205 duplex stainless steel. *Steel Res Int.* 2014;85(5):776-83. <http://dx.doi.org/10.1002/srin.201300293>.
 41. Forgas A Jr, Marangoni J, Otubo J, Donato GHB, Magnabosco R. Reverse strain-induced martensitic transformation of the ferrite to austenite in duplex stainless steels. *J Mater Sci.* 2016;51(23):10452-63. <http://dx.doi.org/10.1007/s10853-016-0265-1>.
 42. Paula Inácio LK, Wolf W, de Leucas BCB, Stumpf GC, Santos DB. Microtexture evolution of sigma phase in an aged fine-grained 2205 duplex stainless steel. *Mater Charact.* 2021;171:110802. <http://dx.doi.org/10.1016/j.matchar.2020.110802>.
 43. Kashiwar A, Vennela NP, Kamath SL, Khatirkar RK. Effect of solution annealing temperature on precipitation in 2205 duplex stainless steel. *Mater Charact.* 2012;74:55-63. <http://dx.doi.org/10.1016/j.matchar.2012.09.008>.
 44. Mao Y, Zheng Y, Shi Y, Zhu M, Saitejin, Liu S, et al. Effect of rolling deformation on microstructure and mechanical properties of 2205 duplex stainless steel with micro-nano structure. *Mod Phys Lett B.* 2020;34(25):1-12. <http://dx.doi.org/10.1142/S0217984920502693>.
 45. Tavares TB, Rodrigues DG, Santos DB. Effect of warm rolling and annealing on microstructure, texture, and mechanical properties of a 2205 duplex stainless steel. *Steel Res Int.* 2020;91(4):1-11. <http://dx.doi.org/10.1002/srin.201900543>.
 46. Maria GGB, Pedrosa CAD, Rodrigues DG, Santos DB. Strain-induced martensite and reverse transformation in 2304 lean duplex stainless steel and its influence on mechanical behavior. *Steel Res Int.* 2019;90(3):1-11. <http://dx.doi.org/10.1002/srin.201800437>.
 47. Breda M, Brunelli K, Grazzi F, Scherillo A, Calliari I. Effects of cold rolling and strain-induced martensite formation in a SAF 2205 duplex stainless steel. *Metall Mater Trans, A Phys Metall Mater Sci.* 2015;46(2):577-86. <http://dx.doi.org/10.1007/s11661-014-2646-x>.
 48. Jinlong L, Tongxiang L, Chen W, Limin D. Effect of ultrafine grain on tensile behaviour and corrosion resistance of the duplex stainless steel. *Mater Sci Eng C.* 2016;62:558-63. <http://dx.doi.org/10.1016/j.msec.2016.02.008>.
 49. Rodrigues DG, Maria GGB, Viana NAL, Santos DB. Effect of low cold-rolling strain on microstructure, texture, phase transformation, and mechanical properties of 2304 lean duplex stainless steel. *Mater Charact.* 2019;150:138-49. <http://dx.doi.org/10.1016/j.matchar.2019.02.011>.
 50. Jinlong L, Guo W, Liang T. The effect of pre-deformation on corrosion resistance of the passive film formed on 2205 duplex stainless steel. *J Alloys Compd.* 2016;686:176-83. <http://dx.doi.org/10.1016/j.jallcom.2016.06.003>.
 51. Mendonça CSP, Matos RAG, Mendes J, Melo MLNM, Rodrigues G, Silva MR, et al. Study of formation and reversion of the martensitic phase induced by deformation of lean duplex stainless steel. *J Nondestruct Eval.* 2018;37(3):1-7. <http://dx.doi.org/10.1007/s10921-018-0518-9>.
 52. Ahmed MZ, Bhattacharjee PP. Microstructure, texture, and tensile properties of a severely warm-rolled and annealed duplex stainless steel. *Steel Res Int.* 2016;87(4):472-83. <http://dx.doi.org/10.1002/srin.201500107>.
 53. Keichel J, Foct J, Gottstein G. Deformation and annealing behavior of nitrogen alloyed duplex stainless steels. Part I: rolling. *ISIJ Int.* 2003;43(11):1781-7. <http://dx.doi.org/10.2355/isijinternational.43.1781>.
 54. Pan M, Zhang X, Chen P, Su X, Misra RDK. Bin, Misra RDK. The effect of chemical composition and annealing condition on the microstructure and tensile properties of a resource-saving duplex stainless steel. *Mater Sci Eng A.* 2020;788:139540. <http://dx.doi.org/10.1016/j.msea.2020.139540>.
 55. Malta PO, Alves DS, Ferreira AOV, Moutinho ID, Dias CAP, Santos DB. Static recrystallization kinetics and crystallographic texture of Nb-stabilized ferritic stainless steel based on orientation imaging microscopy. *Metall Mater Trans, A Phys Metall Mater Sci.* 2017;48(3):1288-309. <http://dx.doi.org/10.1007/s11661-016-3935-3>.
 56. Malta PO, Moutinho ID, Alves DS, Ferreira AV, Santos DB. Recrystallization kinetics and texture evolution of Nb stabilized ferritic 430 stainless steel cold rolled and isothermal annealed. *Mater Sci Forum.* 2017;879:1656-61. <http://dx.doi.org/10.4028/www.scientific.net/MSF.879.1656>.
 57. Llorca-Isern N, López-Luque H, López-Jiménez I, Biezma MV. Identification of sigma and chi phases in duplex stainless steels. *Mater Charact.* 2016;112:20-9. <http://dx.doi.org/10.1016/j.matchar.2015.12.004>.
 58. Moura AN, Favarato LNO, Itman A Fo, Alcântara CM, Cunha MA, Oliveira TR, et al. Study of the recrystallization and crystallographic texture evolution during final annealing of UNS S32304 Lean Duplex stainless steel. *Mater Charact.* 2017;130:39-49. <http://dx.doi.org/10.1016/j.matchar.2017.05.025>.
 59. Li J, Guo J, Lu CY, Jia PG, Wu SH. Mechanical and corrosion behaviors of 25Cr-5.3Ni-2.8Mo-0.15n duplex stainless steel castings affected by annealing process. *Mater Corros.* 2015;66(2):105-10. <http://dx.doi.org/10.1002/maco.201307213>.

60. Luo H, Dong CF, Xiao K, Li XG. Characterization of passive film on 2205 duplex stainless steel in sodium thiosulphate solution. *Appl Surf Sci.* 2011;258(1):631-9. <http://dx.doi.org/10.1016/j.apsusc.2011.06.077>.
61. Jinlong L, Liang T, Wang C, Guo T. Influence of sensitization on passive films in AISI 2205 duplex stainless steel. *J Alloys Compd.* 2016;658:657-62. <http://dx.doi.org/10.1016/j.jallcom.2015.10.246>.
62. Jinlong L, Tongxiang L, Limin D, Chen W. Influence of sensitization on microstructure and passive property of AISI 2205 duplex stainless steel. *Corros Sci.* 2016;104:144-51. <http://dx.doi.org/10.1016/j.corsci.2015.12.005>.
63. Luo H, Dong CF, Li XG, Xiao K. The electrochemical behaviour of 2205 duplex stainless steel in alkaline solutions with different pH in the presence of chloride. *Electrochim Acta.* 2012;64:211-20. <http://dx.doi.org/10.1016/j.electacta.2012.01.025>.
64. Rahimi E, Kosari A, Hosseinpour S, Davoodi A, Zandbergen H, Mol JMC. Characterization of the passive layer on ferrite and austenite phases of super duplex stainless steel. *Appl Surf Sci.* 2019;496:143634. <http://dx.doi.org/10.1016/j.apsusc.2019.143634>.
65. MacDonald DD. The history of the Point Defect Model for the passive state: a brief review of film growth aspects. *Electrochim Acta.* 2011;56(4):1761-72. <http://dx.doi.org/10.1016/j.electacta.2010.11.005>.
66. Fattah-alhosseini A, Vafaeian S. Comparison of electrochemical behavior between coarse-grained and fine-grained AISI 430 ferritic stainless steel by Mott-Schottky analysis and EIS measurements. *J Alloys Compd.* 2015;639:301-7. <http://dx.doi.org/10.1016/j.jallcom.2015.03.142>.
67. Yi G, Xu J, Zheng C. Semiconductor properties of passive film and corrosion resistance of 2205 duplex stainless steel joint welded by laser hybrid welding. *Anti-Corros Methods Mater.* 2019;66(3):327-35. <http://dx.doi.org/10.1108/ACMM-09-2018-2002>.
68. Luo H, Wang X, Dong C, Xiao K, Li X. Effect of cold deformation on the corrosion behaviour of UNS S31803 duplex stainless steel in simulated concrete pore solution. *Corros Sci.* 2017;124:178-92. <http://dx.doi.org/10.1016/j.corsci.2017.05.021>.
69. Cao C. On the impedance plane displays for irreversible electrode reactions based on the stability conditions of the steady-state: I. One state variable besides electrode potential. *Electrochim Acta.* 1990;35(5):831-6. [http://dx.doi.org/10.1016/0013-4686\(90\)90077-D](http://dx.doi.org/10.1016/0013-4686(90)90077-D).
70. Orazem ME, Frateur I, Tribollet B, Vivier V, Marcelin S, Pébère N, et al. Dielectric properties of materials showing Constant-Phase-Element (CPE) impedance response. *J Electrochem Soc.* 2013;160(6):215-25. <http://dx.doi.org/10.1149/2.033306jes>.
71. Orazem ME, Tribollet B, Vivier V, Riemer DP, White E, Bunge A. On the use of the power-law model for interpreting constant-phase-element parameters. *J Braz Chem Soc.* 2014;25:532-9. <http://dx.doi.org/10.5935/0103-5053.20140021>.
72. Man C, Dong C, Kong D, Wang L, Li X. Beneficial effect of reversed austenite on the intergranular corrosion resistance of martensitic stainless steel. *Corros Sci.* 2019;151:108-21. <http://dx.doi.org/10.1016/j.corsci.2019.02.020>.
73. Moulder JF, Stickle WF, Sobol PE, Bomben KD. *Handbook of X-ray photoelectron spectroscopy: a reference book of standard spectra for identification and interpretation of XPS data.* Minnesota: Perkin-Elmer Corporation, Physical Electronics Division; 1992. Data interpretation, quantitative analysis; p. 25-6.